Plasma scale-length effects on electron energy spectra in high-irradiance laser plasmas

O. Culfa,[1,2] G. J. Tallents,[2] A. K. Rossall,[2] E. Wagenaars,[2] C. P. Ridgers,[2] C. D. Murphy,[2] R. J. Dance,[2] R. J. Gray,[3] P. McKenna,[3] C. D. R. Brown,[4] S. F. James,[4] D. J. Hoarty,[4] N. Booth,[5] A. P. L. Robinson,[5] K. L. Lancaster,[2,5] S. A. Pikuz,[6] A. Ya. Faenov,[6,7] T. Kampfer,[8] K. S. Schulze,[8] I. Uschmann,[8] and N. C. Woolsey[2]

[1]*Department of Physics, Karamanoglu MehmetBey University, Karaman, Turkey*

[2]*York Plasma Institute, The Department of Physics, The University of York, York YO10 5DD, United Kingdom*

[3]*SUPA, Department of Physics, University of Strathclyde, Glasgow G4 0NG, United Kingdom*

[4]*AWE, Aldermaston, Reading, Berkshire RG7 4PR, United Kingdom*

[5]*CLF, STFC Rutherford Appleton Laboratory, Didcot, Oxfordshire OX11 0QX, United Kingdom*

[6]*Joint Institute for High Temperatures, Russian Academy of Sciences, Moscow 125412, Russia*

[7]*Osaka University, Suita, Osaka 656-0871, Japan*

[8]*Friedrich Schiller University of Jena, D-07743 Jena, Germany*

(Received 14 September 2015; revised manuscript received 8 February 2016; published 6 April 2016)

An analysis of an electron spectrometer used to characterize fast electrons generated by ultraintense (10^{20} W cm^{-2}) laser interaction with a preformed plasma of scale length measured by shadowgraphy is presented. The effects of fringing magnetic fields on the electron spectral measurements and the accuracy of density scale-length measurements are evaluated. 2D EPOCH PIC code simulations are found to be in agreement with measurements of the electron energy spectra showing that laser filamentation in plasma preformed by a prepulse is important with longer plasma scale lengths (>8 μm).

DOI: 10.1103/PhysRevE.93.043201

I. INTRODUCTION

High power lasers can be focused to irradiances exceeding 10^{21} W cm^{-2} enabling access to regimes of physics [1] and applications not previously possible at lower irradiances. Ultrabright pulses of high-energy electrons, ions, and radiation are produced [2,3] and it is feasible that the fast ignitor approach to laser fusion utilizing fast electrons created at high irradiance could ignite fusion reactions in compressed deuterium-tritium fuel [4]. Laser absorption mechanisms are sensitive to gradients of the density profile. Such gradients are often determined by laser prepulses, which are difficult to reduce below the irradiance threshold ($<10^9$ W cm^{-2}) for plasma production due to the necessary high laser contrast ($>10^{11}$) associated with the high irradiance. Plasma mirrors for the incoming laser light have been utilized to increase the laser contrast so as to enable high power laser irradiance onto essentially unperturbed solid target surfaces [5,6]. Alternatively, the production of high-energy electrons, ions, and radiation can be enhanced by deliberately creating gradients of density [7–10]. Culfa *et al.* [11] measured the changes of fast electron temperatures and the number of fast electrons with varying plasma scale length. A well-defined density scale length was created by utilizing a deliberate prepulse before the high-irradiance pulse.

Experimentally measured variations of fast electron numbers and temperatures with plasma scale length are to be expected. Laser absorption processes are known to have strong dependence on the plasma scale length. Resonance absorption [12] exhibits an optimum absorption with varying density scale length, while vacuum heating [13] ceases once the scale length exceeds the electromagnetic field skin depth. The process of $\mathbf{J} \times \mathbf{B}$ electron acceleration in the laser field is enhanced with longer underdense pulse propagation. Laser pulse propagation in longer scale lengths can also be modified by self-focusing [14,15] and other effects, including channel formation [16] which affects the energy coupling to electrons.

In this article, we examine in more detail measurements reported by Culfa *et al.* [11] of electron energies obtained with a circularly shaped magnetic-field spectrometer and measurements of plasma scale lengths obtained with a shadowgraphy technique. The electron spectra recorded as a function of plasma scale length are, in addition, simulated with a two-dimensional PiC code [17,18]. Good agreement of the experimentally measured electron temperatures as a function of scale length is obtained, including the correct scale length giving a maximum temperature. In agreement with the recent results of Gray *et al.* [9], a rollover of the observed temperature increase with increasing scale length is found to be due to filamentation of the radiation before it reaches the critical density region. The measurements and simulations show that it is possible to enhance and control high-irradiance laser energy coupling to fast electrons by controlling the plasma density gradient via control of a deliberate laser prepulse.

The Vulcan laser system at the Rutherford Appleton Laboratory (RAL) has been utilized for these measurements. The petawatt laser delivers 1.054-μm wavelength laser pulses of $\sim$1 ps duration and pulse energies 150 ± 20 J with an intensity contrast of 10^8. Laser irradiance of 10^{20} W cm^{-2} in a p-polarized beam was incident at a 40° angle to a plane target normal. A 5-ns longer duration prepulse was incident at 17° incidence angle with peak irradiance 1.5 ns prior to the main pulse. The petawatt laser was focused onto plane foil of parylene-N (CH) in various thicknesses from 6 to 150 μm. The targets contained a thin (100 nm) layer of aluminium buried at depths $\geqslant 3$ μm from the target surface. The experiment setup is schematically illustrated in Fig. 1.

II. ELECTRON ENERGY MEASUREMENTS

An electron spectrometer was used to measure the energy spectra of electrons created during the high-irradiance irradiation of solid targets. The spectrometer was placed behind

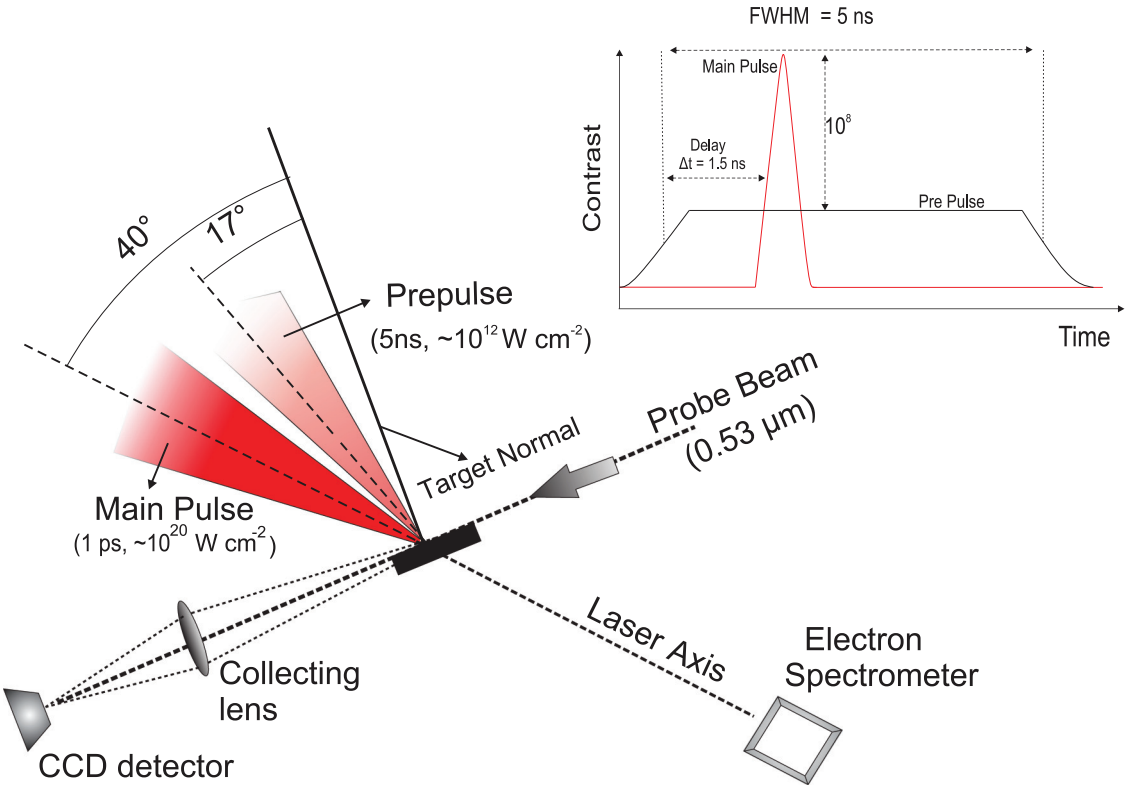

FIG. 1. Experimental setup in the Vulcan Petawatt Laser Facility for the measurement of electron spectra along the laser axis and density gradients normal to the target surface. The inset shows the timing of a prepulse used to modify the interaction density scale length.

the target in line with the high power laser axis (see Fig. 1). Measurements of the range of angles of accelerated electrons using copper wedges and image plates show that with longer scale length ($L \approx 5\ \mu$m) electrons with energies >10 MeV are predominantly accelerated in the laser direction [19,20]. An examination of the energy dispersion of electrons including fringing field effects and the recording of electron fluxes is presented in this section.

A. Dispersion of electrons by a circular magnetic field

The electron spectrometer consists of a permanant magnet with circular pole pieces of radius $R = 2.54$ cm producing a uniform magnetic field between the pole pieces of $B_{\text{spec}} = 0.15$ T. The electrons are deflected by the magnetic field onto a detector plane with image plate detector (see Fig. 2) so that the degree of deflection is inversely proportional to the electron energy in the relativistic limit [21].

The magnetic field of the spectrometer deflects energetic electrons due to the Lorentz force acting on the electrons (see Fig. 2). The rate of change of the electron momentum $\mathbf{p}$ with time is such that

$$\frac{d\mathbf{p}}{dt} = \frac{-e}{\gamma m_e}\mathbf{p} \times \mathbf{B}_{\text{spec}}, \tag{1}$$

where e is the electron charge, m_e is the electron rest mass, and γ is the relativistic mass increase. We assume $\mathbf{y}$ is the initial electron propagation direction, $\mathbf{z}$ is the magnetic field direction (into the page in Fig. 2), and $\mathbf{x}$ is the direction along the detection plane (aligned normally to $\mathbf{y}$).

The magnetic field within the pole pieces of radius R is taken to be given by

$$\mathbf{B_z}(\mathbf{r_b}) = \begin{cases} B_{\text{spec}}\mathbf{z} & (r_b \leqslant R), \\ 0 & (r_b > R), \end{cases} \tag{2}$$

where r_b is the radius from the center of the magnetic pole pieces.

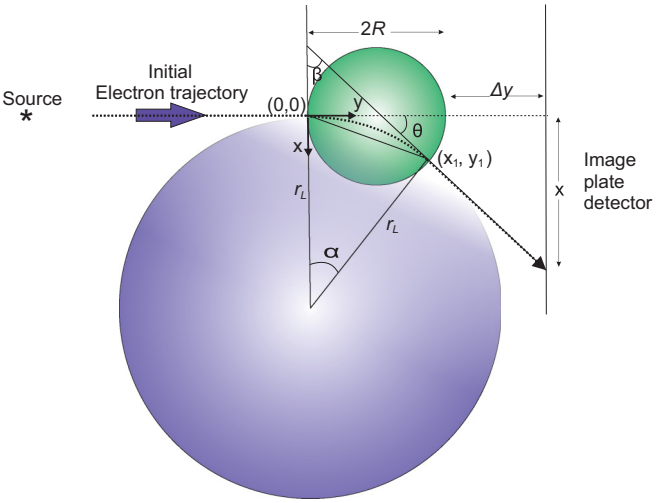

FIG. 2. A schematic of the electron trajectory on passing through the magnetic field directed into the page (small circle) of the electron spectrometer. The big circle circumference represents the Larmor orbit of the electron in the magnetic field.

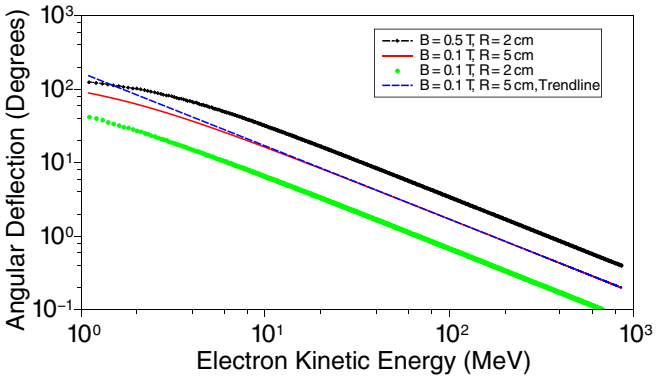

FIG. 3. The angular deflection θ of electrons passing through a magnetic field of strength as shown with circular pole pieces of radius (as shown). The linear dashed line shows the angular deflection angle $\theta \propto 1/E$ trend line for the given values on the graph. The deflection angle θ is approximately inversely proportional to the electron energy E and depends on the B magnetic-field amplitude and R the radius of the magnetic field.

Figure 2 shows the electron trajectory and the magnetic-field position and the Larmor radius which is used to obtain an analytic solution of the electron dispersion. An electron follows a path within the magnetic field with Larmor orbit radius r_L in the x-y plane such that

$$r_L = \frac{p}{eB_{\text{spec}}}. \tag{3}$$

Equation (3) is valid for both relativistic and nonrelativistic electrons.

An exact expression for the dispersion distance x_d along the detection plane neglecting fringing fields can be found. We have that

$$x_d = \left[2R + \Delta y - \frac{2R}{1+\left(\frac{R}{r_L}\right)^2}\right]\tan(\theta) + \frac{2R^2}{r_L}\frac{1}{1+\left(\frac{R}{r_L}\right)^2}, \tag{4}$$

where θ is the angular deflection.

Figure 3 indicates the relationship between electron energy and angular deflection for three different magnetic fields and magnetic-field radii calculated using Eq. (4). In each case, the deflection angle θ is close to being inversely proportional to the electron energy. We have that $\theta \propto 1/E$ for small angle deflections ($<40^\circ$). The dispersion of the magnet changes linearly with the field radius R and field amplitude B_{spec} (proportionally to RB_{spec}).

Assuming $r_L \gg R$, Eq. (4) can be written as

$$x_d \cong \frac{2R}{r_L}[R + \Delta y]. \tag{5}$$

The accuracy of the approximation that $r_L \gg R$, is examined in Fig. 4. We see that the error in neglecting the cylindrical shape of the magnetic pole pieces is less than 3% for energies greater than 25 MeV. In the nonrelativistic limit, applying the Larmor radius $r_L = \frac{m_e v}{eB}$ to Eq. (5) and writing v in terms of energy (E) gives

$$x_d = \sqrt{2}\,R(R + \Delta y)\,\frac{eB}{m_e^{1/2}E^{1/2}}. \tag{6}$$

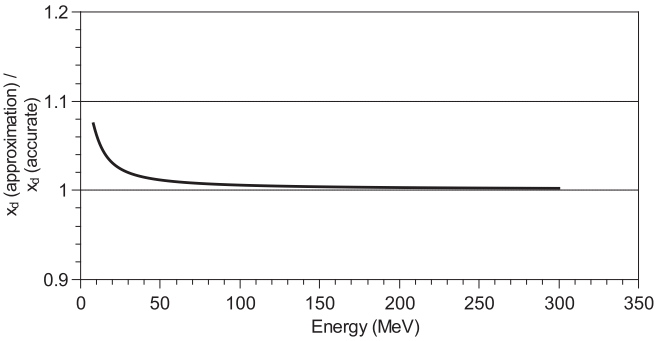

FIG. 4. The approximate dispersion distance x_d is compared to the accurate x_d dispersion values for highly relativistic electron energies.

This result has also been determined by, for example, Lezius *et al.* [22].

For highly relativistic electrons, we use the Larmor radius given by Eq. (3). Applying the relativistic approximation $E = pc$ gives the result for x_d that

$$x_d = 2R(R + \Delta y)\frac{ecB}{E}. \tag{7}$$

This shows that the dispersion is inversely proportional to the electron energy E in the relativistic regime (see Fig. 5).

So far, the dispersion of the electron spectrometer has been calculated without taking into account a fringing field created by the magnet. We now consider the effect of the fringing magnetic field which is produced on the edge of the magnets. In the design of the electron spectrometer, a yoke has been used to reduce unwanted fringe fields pointing in the opposite direction of the magnetic field between the pole pieces [21]. The electrons are consequently only affected by a magnetic field in the same direction as the magnetic field between the pole pieces before entering and after leaving the space between the pole pieces. A single axis hall probe was used to map the magnetic field of the electromagnet (see Fig. 6).

The dispersion of electrons is increased by taking into account the effect of fringing magnetic fields. The effect of the variation of electron momentum perpendicular to the initial

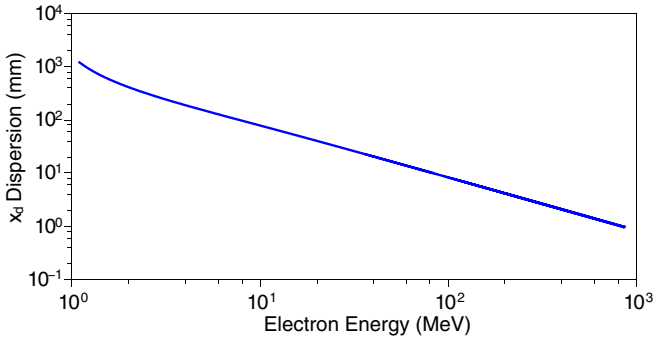

FIG. 5. The dispersion x_d of electrons passing through the electron spectrometer. Their dispersion distance is approximately inversely proportional to the electron energy $x_d \propto 1/E$. A magnetic field of $B_{\text{spec}} = 0.15$ T is applied to the electrons (with $R = 2.54$ cm, $\Delta y = 31.5$ cm).

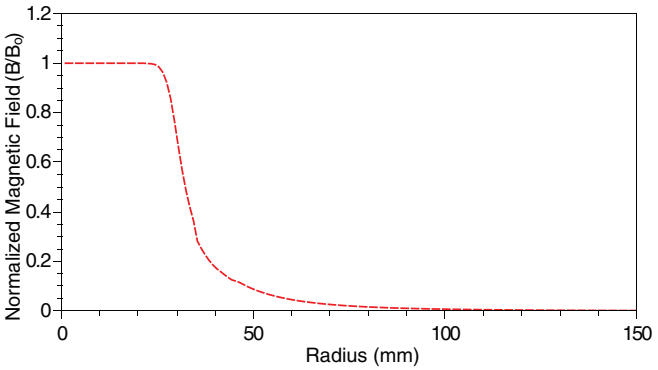

FIG. 6. Measured magnetic field for the electron spectrometer as a function of radius from the center of the electromagnet.

direction of electron momentum due to a fringing field can be obtained by integrating over the fringing magnetic field. To a good approximation, the change in electron momentum due to the fringing field $B(y)$ is given by

$$\Delta p = \frac{-e}{m\gamma}\frac{p}{c}\int B(y)dy \tag{8}$$

assuming that the electrons are relativistic with $dy = cdt$ and the integration is over the fringing field.

From the spectrometer to the image plate detector, we have for relativistic electrons an electron momentum in the direction of the electron dispersion given by

$$\Delta p_x(out) = -e\int_R^{\Delta y} B(y)dy, \tag{9}$$

while from the target to the spectrometer, we have

$$\Delta p_x(in) = -e\int_R^{L_t} B(y)dy, \tag{10}$$

where L_t is the distance from the edge of the spectrometer pole piece to the target.

The total effect on the spectrometer dispersion Δx of the fringing field is given by

$$\Delta x = \frac{\Delta p_x(out)\Delta y}{p_y} + \frac{\Delta p_x(in)(\Delta y + 2R)}{p_y}. \tag{11}$$

Integrating the fringing field of Fig. 6 shows that the fringing field of the electromagnets causes an additional dispersion Δx, such that $\Delta x/x_d \backsimeq 0.4$, where x_d is the dispersion calculated neglecting fringing fields. For the calculations of electron energy spectra a total dispersion distance such that

$$x_d(\text{total}) = x_d + \Delta x \tag{12}$$

is used.

Figure 7 shows the relationship between electron energy and the total dispersion of electrons for our electron spectrometer (with $R = 2.54$ cm, $B_{\text{spec}} = 0.15$ T, $\Delta y = 31.5$ cm) calculated using Eqs. (3), (4), and (12). In the relativistic regime, where the energy $E \gg 0.511$ MeV, Fig. 7 shows that $x_d(\text{total}) \propto \frac{1}{E}$ in agreement with Eqs. (7) and (12). Our calculations indicate that the relativistic assumption [Eq. (12)] is accurate for energies $E > 2$ MeV. In practical units, we have

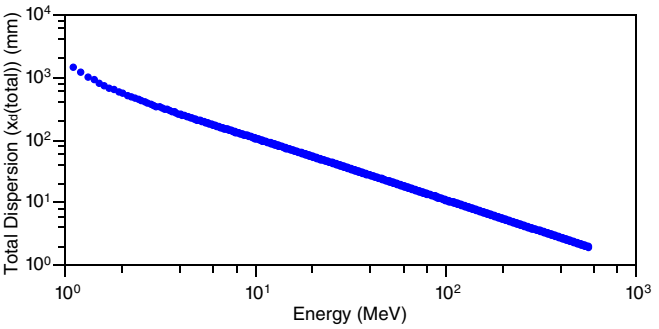

FIG. 7. The total dispersion $x_d(\text{total})$ of electrons passing through the electron spectrometer when the fringing field is taken into account. A magnetic field of $B_{\text{spec}} = 0.15$ T is applied to the electrons (with $R = 2.54$ cm, $\Delta y = 31.5$ cm).

from Eq. (12) that

$$x_d(\text{total})(\text{mm}) = \frac{1025.5}{E(\text{MeV})}. \tag{13}$$

B. Electron detection measurements

Electrons were detected using image plates (Fuji film BAS-SR 2025 [23,24]). Electron detection on the image plates is caused by photostimulated luminescence (PSL). The image plate is read using a scanner (FLA 5000) [23]. The surface of the image plate is scanned by visible lasers of wavelength suitable for further excitation of the metastable states generating PSL radiation which is read by a photomultiplier tube (PMT) which converts the optical signal in an electric signal. The spatial resolution is generally 25–50 μm. Previous experiments show that image plates accurately measure the total electron energy impinging on the plates [25–28].

Figure 8 shows the unprocessed signal of the electron energy spectra obtained during the experiment. The big bright spot marked on the axis is caused by energetic protons. If we magnify this region (within the white circle on Fig. 8), there is another bright spot marked on the axis caused by x

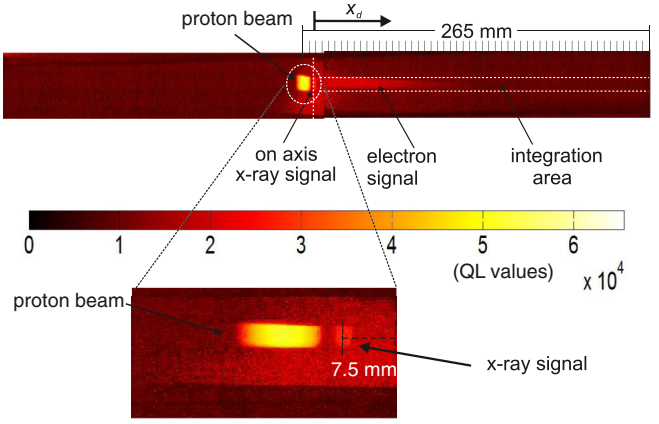

FIG. 8. An example of an image plate image showing detected electron signals (with a scale length of 11.1 μm.) The center of the bright spot shows the deposited energy due to x rays. The electron signal is on the right-hand side. On the distance scaling each grid point corresponds to 5 mm distance.

rays produced during the interaction which pass through the spectrometer collimator. The midpoint of this x-ray beam is accepted as the position of infinite electron energy and used to calculate the electron energy dispersion. A clear signal stripe is seen on the right side of the central axis due to electrons which have been deflected by the magnetic field. The marked area within the dashed line on Fig. 8 is integrated vertically in order to produce an electron energy spectrum after a subtraction of the background exposure. Errors involved in measuring electron energies have been discussed by Culfa *et al.* [11].

III. MEASUREMENTS OF PLASMA SCALE LENGTH

Using a controlled prepulse creates a preformed plasmas in front of the target surface. The density scale length of the preplasma determines the interaction physics of the main high-irradiance laser pulse. We describe a shadowgraphy technique used to determine the preplasma density scale length in our experiment. The prepulse was created by a 5-ns pulse incident 1.5 ns before the main short pulse. The peak laser irradiance varied over a range 1.8×10^{12}–2.5×10^{12} W cm^{-2} which along with focusing variations produced varying density scale lengths which were measured at the time of incidence of the short high-irradiance laser pulse.

Refraction of probing rays along the target surface depends on the electron density gradient. Consider a slab of plasma with two rays passing through a distance dz apart. The optical path length difference between the two rays is $\lambda\frac{d\phi}{2\pi}$ where λ is the wavelength of the probe light and $d\phi$ is the phase difference. The direction of propagation beam is perpendicular to the resultant phase front, so the angle of diffraction is

$$\theta = \frac{\lambda\frac{d\phi}{2\pi}}{dz} = \frac{d}{dz}\int N dl, \tag{14}$$

where N is the plasma refractive index.

A frequency doubled optical probe beam was used to record the expansion profile of the plasma at the time of the interaction pulse. The probe beam was directed parallel to the target surface passing through the plasma produced by the longer pulse laser target interaction. Figure 9 shows the experimental setup for the shadowgraphy technique.

Assuming the electron density at the original target surface is given by $n_s = Z/(m_p M)\rho$, where ρ is the solid target mass density, $Z^* \cong 6$ is the average charge, M is the atomic mass of the largely carbon target, and m_p is the proton mass, we can determine the density scale length L from the measurement of $\theta_{\max}$. We also assume an exponential electron density gradient such that the electron density varies with distance z from the solid target surface such that

$$n_e(z) = n_s \exp\left(-\frac{z}{L}\right), \tag{15}$$

where L is the electron density scale length. The rays initially parallel to the target surface are deflected by angle [29,30]

$$\theta = \frac{n_e(z)}{2n_c}\frac{\Delta y}{L} \tag{16}$$

for a uniform plasma of width Δy. Here n_c is the critical density for the probing radiation. We assume that $n_e(z) \ll n_c$,

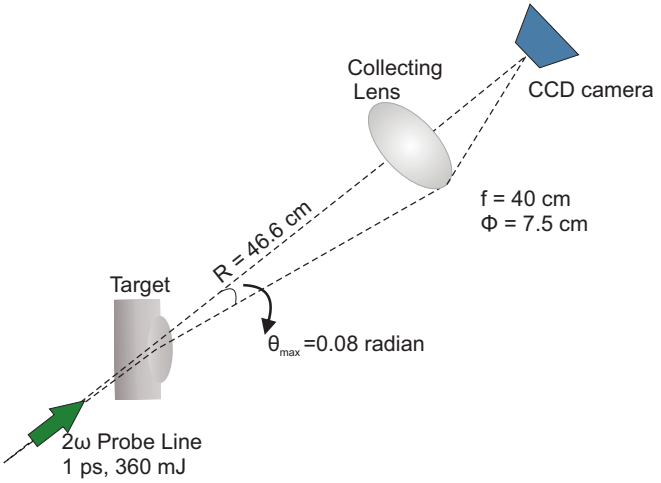

FIG. 9. Optical probing shadowgraphy experimental setup. The probe line passes through a refracting plasma and images cannot be detected for more than the maximum refraction angle 0.08 radian determined by the lens.

so that the plasma refractive index is given by $1 - \frac{n_e(z)}{2n_c}$. For our experiment described with beam imaging optics of $f/5.3$, rays of angle $\theta > \theta_{\max} = 0.08$ radian are not detected. Plasma regions where $\theta > \theta_{\max}$ appear black in the shadowgrams.

Figures 10 and 11 show an examples of shadowgraph images taken during the experiment. The shadowgraphy technique allows quantitative information on the scale lengths of the probed plasmas and enables the visualization of the geometry of the generated plasma (see Figs. 10 and 11).

Equation (16) has a dependence on scale length L and electron number density $n_e(z)$. We can write that

$$\theta_{\max} = \frac{z_{\max}}{n_s}\frac{\Delta y}{L} = \frac{z_{\max}}{L}\exp\left(-\frac{z_{\max}}{L}\right), \tag{17}$$

where $z_{\max}$ is the distance from the original target surface on the shadowgrams (e.g., Figs. 10 and 11) corresponding to the maximum detected refraction angle $\theta_{\max}$ (the extended black region). We know all quantities on the left-hand side of Eq. (17), so we can determine the appropriate $\frac{z_{\max}}{L}$ value and hence scale length L from Fig. 12.

Two values of scale length L in Fig. 12 produce the same refraction angle: a high density and long scale length and lower density and shorter scale length. Given the time scale for plasma expansion due to the prepulse ($\Delta t = 1.5$ ns), the longer scale-length solution ($L \simeq 1$–11 μm) is assumed as we expect $L \sim v_s \Delta t$, with v_s ($\sim10^3$ m s^{-1}) the sound speed.

Refraction effects can cause errors in our measured value of $z_{\max}$. A schematic illustration of probe refraction is given in Fig. 13. A lens focused on the target position collects light from the probe beam. Focusing by the lens reduces the error in measuring $z_{\max}$. We examine the error on the measurements of $z_{\max}$ by the following analysis.

The equation of the probe ray initially incident out at $z = \Delta z$ can be shown to be given by

$$z = \frac{\Delta y}{2}\tan^{-1}(\theta_{\max}) \tag{18}$$

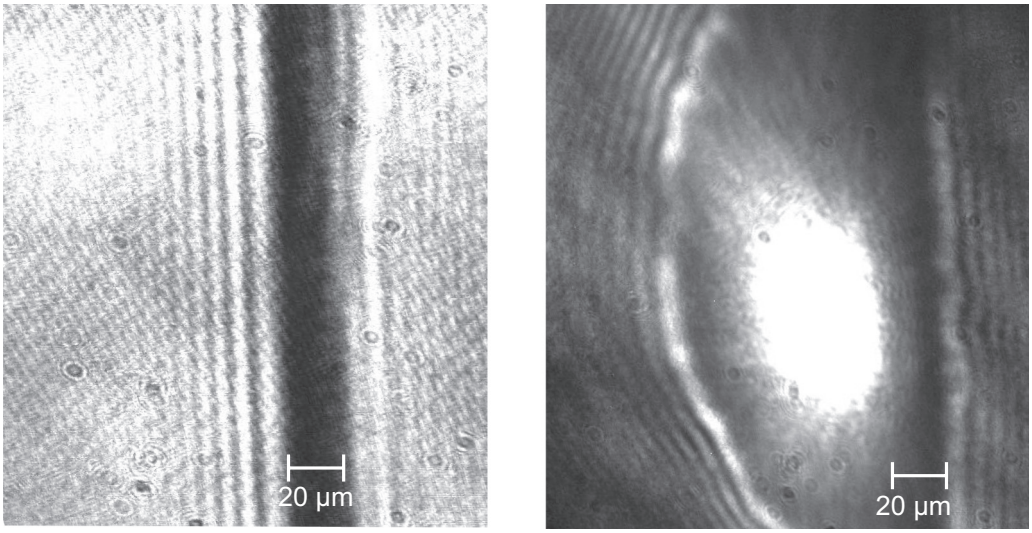

FIG. 10. An example of shadowgraph, showing generated plasma after the laser shot. Panel (a) shows the reference target before the shot and (b) shows the same target after the shot irradiated by 2.2×10^{12} W cm^{-2} prepulse and 3.8×10^{20} W cm^{-2} main pulse intensity. Panel (b) is taken at the time of peak laser irradiance.

The broken line in Fig. 13 shows the apparent position on the ray, so that the positional difference between the apparent position and actual position is

$$\Delta z_{\text{error}} = -\frac{\Delta y}{2}\tan^{-1}(\theta_{\max}). \tag{19}$$

This position error reflects the error in measuring $z_{\max}$ from the shadowgrams (Figs. 10 and 11). We have typical $\Delta z_{\text{error}}/z_{\max} \simeq 0.1$.

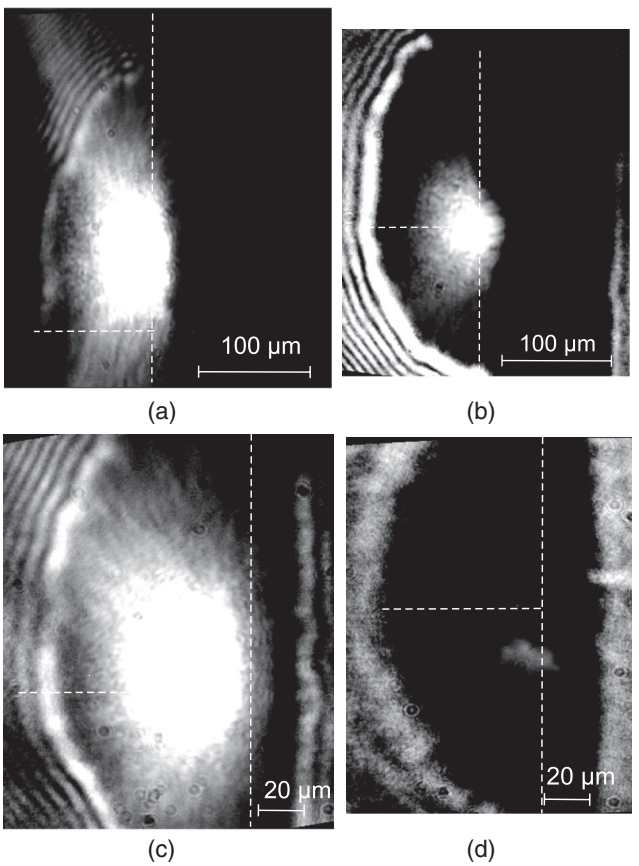

FIG. 11. Sample shadowgraphy images for different scale lengths (a) 11.1 μm, (b) 9 μm, (c) 7.2 μm, (d) 6 μm. The vertical broken line indicates the initial target surface.

IV. COMPARISON OF ENERGY SPECTRA WITH EPOCH 2D PIC CODE SIMULATIONS

The 1D PIC code ELPS and 2D PIC code EPOCH [18] were used to simulate the experimental electron spectra. The 1D code which was used in the presented work is known as the Entry Level PIC Simulation (ELPS) [31]. For the 1D code (ELPS), 7×10^5 spatial points were used with a cell size of 1×10^{-9} m. A 20-μm CH foil target with exponential density profile and scale length L was varied from 1 to 11 μm. There were ten particles of electron and ions in each cell. A Gaussian laser pulse shape was chosen with an intensity of

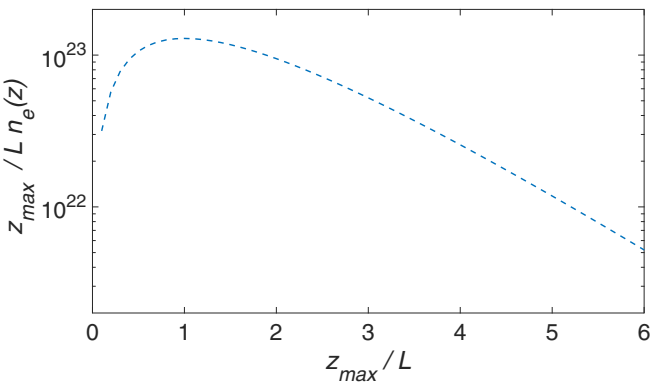

FIG. 12. The value of the right-hand side of Eq. (17) $[\frac{z_{\max}}{L}\exp(-\frac{z_{\max}}{L})]$ as a function of $\frac{z_{\max}}{L}$.

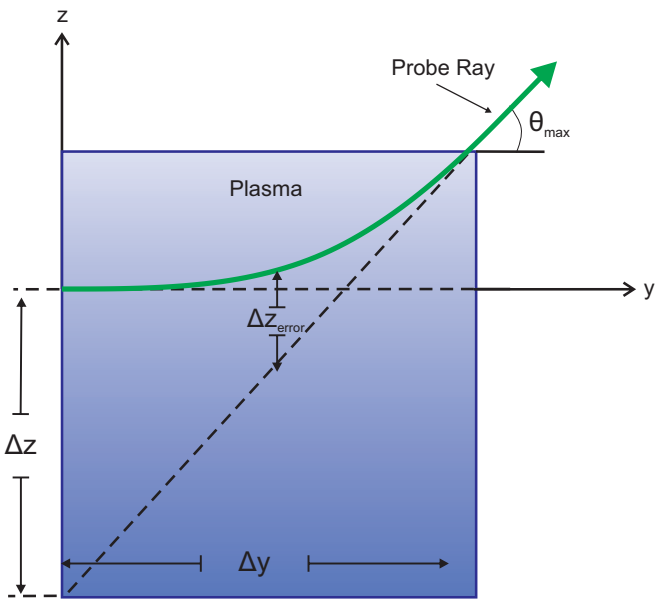

FIG. 13. Schematic illustration of refraction of a probe beam in a planar plasma (uniform in the probing beam direction). The density is assumed to decrease with increasing z and to be uniform in y.

5×10^{20} W cm^{-2}. Laser wavelength and pulse duration were 1 μm and 1 ps, respectively.

For the 2D code, the system size was 90 μm $\times$ 90 μm with a mesh resolution of 1500$\times$1500 cells with 16 particles of electrons and protons in a cell. The experimental variation of electron energy spectra for different scale lengths with the laser irradiance of 5×10^{20} W cm^{-2} focused on a 7-μm focal spot with an incidence angle of 40° was determined. The laser wavelength and pulse duration were 1 μm and 1 ps, respectively.

In the simulations, the peak electron density was limited at $100n_c$ where n_c is the critical density. An exponential density profile was assumed with varying scale lengths L from 1 to 11 μm with a out off to zero density at $0.01n_c$.

The hot electron energy spectrum can be extracted from the simulation. The electron energy spectra was extracted at 0.5 ps after the laser has delivered all of its energy to the electrons. Figure 14 compares the generated electron spectra from the 2D PIC code to the experimental electron energy spectra for different scale lengths. The dots represent the EPOCH 2D PIC code simulation results and continuous line shows our experimental observations.

Previous work [32,33] shows that space charges generated at the target during laser irradiation have an effect on the lower electron energies recorded by electron spectrometer at some distance from the target. The space charge generated electric field E has been shown [32,33] to be related to the hot electron temperature T_e by

$$E = \frac{T_e}{eL}, \tag{20}$$

where L is the local plasma scale length. Hot electrons under an energy equivalent to the electron temperature are not experimentally observed due to the space charge sheath effect close to the target [32,33].

At the high irradiances (10^{20} W cm^{-2}) of our experiment, electrons are expelled from the laser propagation axis due to

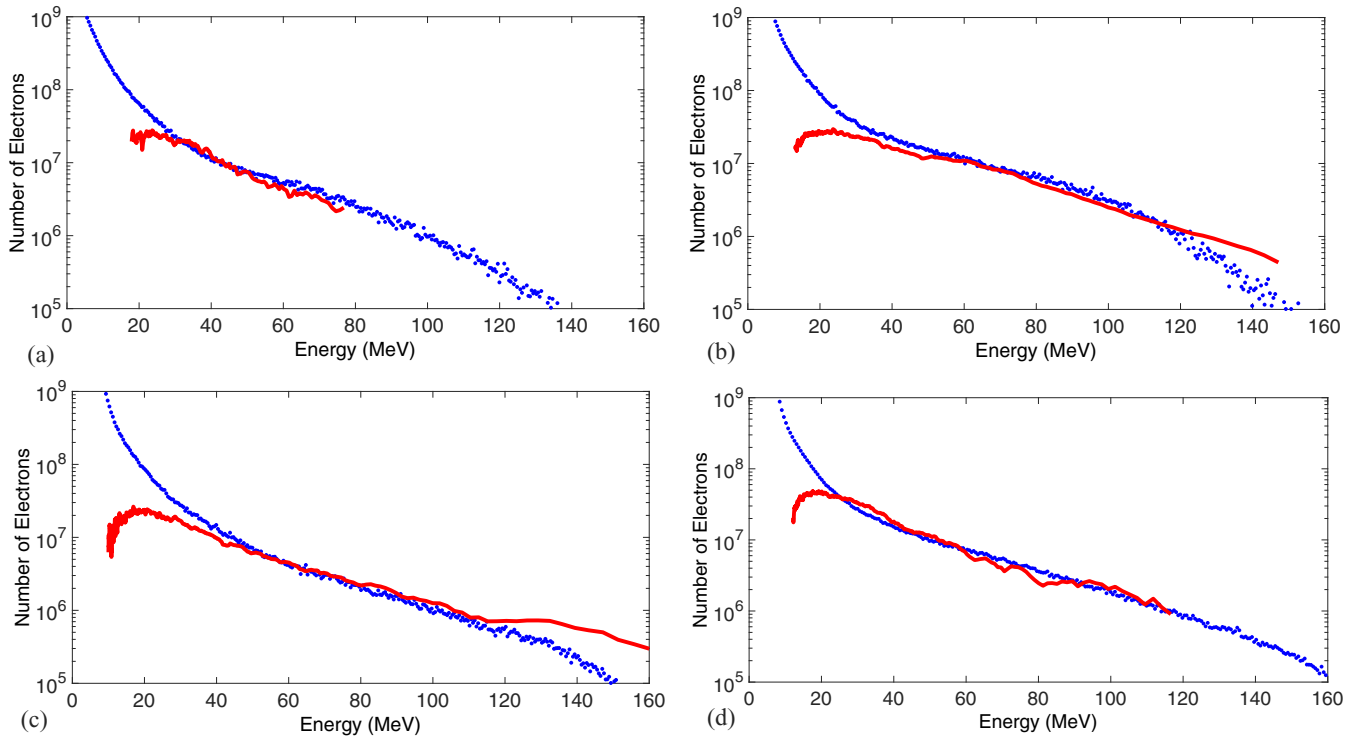

FIG. 14. Comparison of EPOCH 2D PIC code results with experimental electron spectra for (a) 6 μm, (b) 7.5 μm, (c) 9 μm, and (d) 11 μm scale length. The continuous line decreasing at low energy due to target space charge effects represents the experimental data, while the dotted points are the simulation results. The vertical scales are arbitrary and the experimental and simulated spectra are visually superimposed.

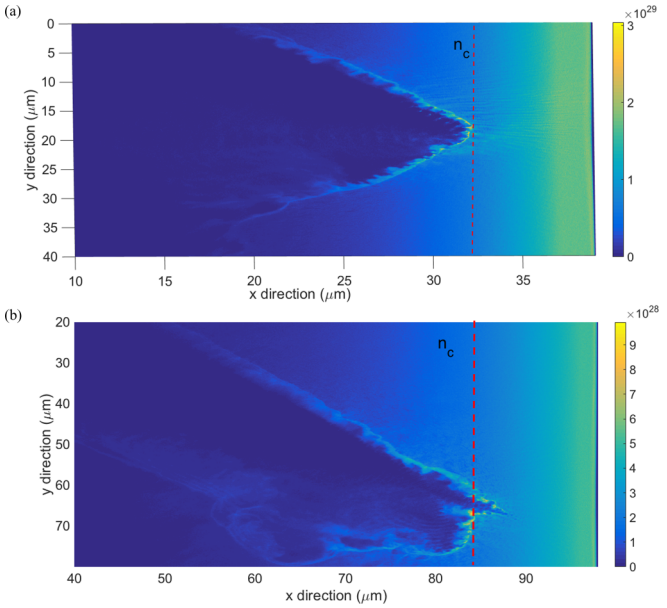

FIG. 15. An example of electron density profile after 0.55 ps with (a) 5-μm, (b) 11-μm scale length as simulated by the EPOCH 2D PIC code. The dashed vertical line indicates the critical density surface. The laser radiation is incident at 40° to the target normal.

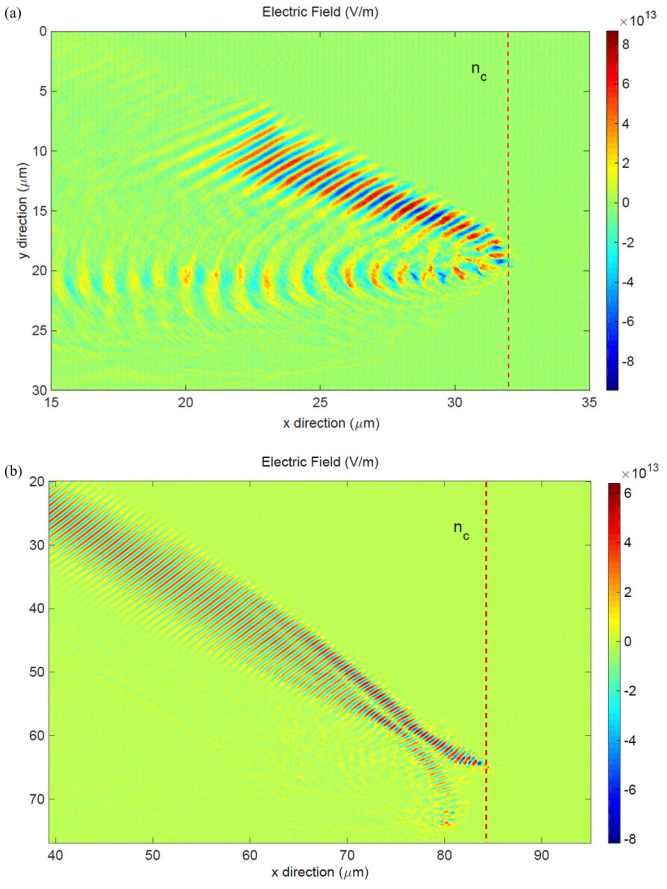

FIG. 16. An example of laser electric field profile after 0.55 ps with (a) 5-μm, (b) 11-μm scale length as simulated by the EPOCH 2D PIC code. The dashed vertical line indicates the critical density surface. The laser radiation is incident at 40° to the target normal.

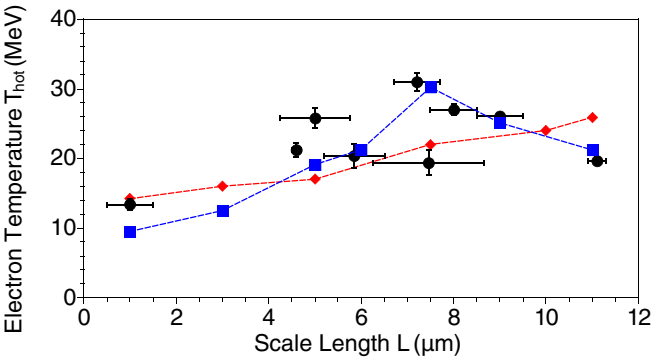

FIG. 17. Experimental measurements of electron temperature as a function of the measured plasma scale length for a number of individual laser shots (circles). Superimposed are one-dimensional (1D) (diamonds) and 2D (squares) PIC code simulations with the preformed scale length and following experimental parameters.

the ponderomotive force. The plasma refractive index on axis is increased due to the electron density drop which produces a positive lensing effect [15]. Laser pulses also undergo self-focusing due to relativistic mass increase of the electrons accelerated by high-irradiance laser light [34]. The transverse ponderomotive force can be sufficiently large to expel a significant fraction of the electrons from the high intensity laser region, creating an ion channel (see Fig. 15). With the longer plasma propagation distances associated with longer plasma scale lengths, the laser pulse can be subject to transverse instabilities, resulting in beam filamentation (see Fig. 16). The filamentation reduces the local laser irradiance and reduces the temperature of accelerated electrons (as seen in Fig. 17).

Figure 16 shows the laser electric field profile predicted by the PIC code simulation after 0.55 ps with a (a) 5-μm and (b) 11-μm scale length. It is seen that for the 5-μm scale length, the laser is reflected at the critical density and does not filament [see Fig. 16(a)] which explains why the hot electron temperature increases for shorter scale lengths ($L < 7.5$ μm). At longer scale lengths ($L > 7.5$ μm), the laser energy is absorbed before the critical density and starts to filament [see Fig. 16(b)] which explains why the electron temperature decreases with longer scale lengths ($L > 7.5$ μm).

Figure 17 summarizes the results for the electron temperature as a function of generated scale length. Experimental observations are shown with circles, 1D PIC code results are presented by diamonds, and 2D PIC simulations are given by squares. It is clear that the 2D PIC code simulations are in good agreement with our experimental observations.

V. CONCLUSION

An analysis of an electron spectrometer has been presented including the effect of fringing magnetic-field effect. We have presented the measurements of the temperature of hot electrons obtained using the electron spectrometer. The results have been correlated to the density scale length of the plasma produced by a controlled prepulse measured using an optical probe diagnostic. Detailed analysis of the density scale-length measurements have been given and error calculations due to the refraction of probe beam have been calculated. 1D PIC simulations

predict electron temperature variations with plasma density scale length in approximate agreement with the experiment at shorter scale lengths (<7.5 μm), but were not able to predict the measured electron temperatures at longer scale lengths. The experimentally observed electron temperature decreases for longer scale lengths as predicted by a 2D PIC code. The agreement of the experimental and 2D simulation results at longer scale length shows that two-dimensional effects affect the laser interaction and electron temperatures [9].

ACKNOWLEDGMENTS

The authors gratefully acknowledge the assistance of laser operations, target preparation, and engineering staff at the Central Laser Facility of RAL. Part of the research was supported by RFBR Research Project No. 15-32-21121 and RAS Presidium Program for Basic Research No. 13. This work was in part funded by the UK EPSRC Grants No. EP/G054950/1, No. EP/G056803/1, No. EP/G055165/1, and No. EP/M022463/1.

[1] M. Tabak, J. Hammer, M. E. Glinsky, W. L. Kruer, S. C. Wilks, J. Woodworth, E. M. Campbell, M. D. Perry, and R. J. Mason, Phys. Plasmas **1**, 1626 (1994).
[2] H. Daido, M. Nishiuchi, and A. S. Pirozhkov, Rep. Prog. Phys. **75**, 056401 (2012).
[3] A. Macchi, M. Borghesi, and M. Passoni, Rev. Mod. Phys. **85**, 751 (2013).
[4] M. H. Key, E. M. Campbell, T. E. Cowan, S. P. Hatchett, E. A. Henry, J. A. Koch, A. B. Langdon, B. F. Lasinski, A. MacKinnon, A. A. Offenberger, D. M. Pennington, M. D. Perry, T. J. Phillips, T. C. Sangster, M. S. Singh, R. A. Snavely, M. A. Stoyer, M. Tsukamoto, K. B. Wharton, and S. C. Wilks, J. Fusion Energy **17**, 231 (1998).
[5] B. Dromey, S. Kar, M. Zeph, and P. Foster, Rev. Sci. Ins. **75**, 645 (2004).
[6] D. Neely, P. Foster, A. Robinson, F. Lindau, O. Lundh, A. Persson, C.-G. Wahlström, and P. McKenna, Appl. Phys. Lett. **89**, 021502 (2006).
[7] A. J. Mackinnon, M. Borghesi, S. Hatchett, M. H. Key, P. K. Patel, H. Campbell, A. Schiavi, R. Snavely, S. C. Wilks, and O. Willi, Phys. Rev. Lett. **86**, 1769 (2001).
[8] A. Levy, R. Nuter, T. Ceccotti, P. Combis, M. Drouin, L. Gremillet, P. Monot, H. Popescu, F. Reau1, E. Lefebvre, and P. Martin, New J. Phys. **11**, 093036 (2009).
[9] R. J Gray, D. C Carroll, X. H. Yuan, C. M. Brenner, M. Burza, M. Coury, K. L. Lancaster, X. X. Lin, Y. T. Li, D. Neely, M. N. Quinn, O. Tresca, C.-G. Wahlstrom, and P. McKenna, New J. Phys. **16**, 113075 (2014).
[10] P. McKenna, D. C. Carroll, O. Lundh, F. Nurnberg, K. Markey, S. Bandyopadhyay, D. Batani, R. G. Evans, R. Jafer, Saty Kar, D. Neely, D. Pepler, M. N. Quinn, R. Redaelli, M. Roth, C. G. Wahlstrom, X. H. Yuan, and M. Zepf, Laser Part. Beams **26**, 591 (2008).
[11] O. Culfa, G. J. Tallents, E. Wagenaars, C. P. Ridgers, R. J. Dance, A. K. Rossall, R. J. Gray, P. McKenna, C. D. R. Brown, S. F. James, D. J. Hoarty, N. Booth, A. P. L. Robinson, K. L. Lancaster, S. A. Pikuz, A. Ya. Faenov, T. Kampfer, K. S. Schulze, I. Uschmann, and N. C. Woolsey, Phys. Plasmas **21**, 043106 (2014).
[12] W. L. Kruer, *The Physics of Laser Plasma Interactions* (Addison- Wesley, Redwood City, CA, 1988).
[13] F. Brunel, Phys. Rev. Lett. **59**, 52 (1987).
[14] A. G. Litvak, Sov. Phys. JETP **30**, 344 (1969).
[15] C. Max, J. Arons, and A. B. Langdon, Phys. Rev. Lett. **33**, 209 (1974).
[16] Z. Najmudin, K. Krushelnick, M. Tatarakis, E. L. Clark, C. N. Danson, V. Malka, D. Neely, M. I. K. Santala, and A. E. Dangor, Phys. Plasmas **10**, 438 (2003).
[17] J. M. Dawson, Rev. Mod. Phys. **55**, 403 (1983).
[18] T. D. Arber, K. Bennett, C. S. Brady, A. Lawrence-Douglas, M. G. Ramsay, N. J. Sircombe, P. Gillies, R. G. Evans, H. Schmitz, A. R. Bell, and C. P. Ridgers, Plasma Phys. Controlled Fusion **57**, 113001 (2015).
[19] M. I. K. Santala, E. Clark, I. Watts, F. N. Beg, M. Tatarakis, M. Zepf, K. Krushelnick, A. E. Dangor, T. McCanny, I. Spencer, R. P. Singhal, K. W. D. Ledingham, S. C. Wilks, A. C. Machacek, J. S. Wark, R. Allott, R. J. Clarke, and P. A. Norreys, Phys. Rev. Lett. **84**, 1459 (2000).
[20] R. J. Gray, X. H. Yuan, D. C. Carroll, C. M. Brenner, M. Coury, M. N. Quinn, O. Tresca, B. Zielbauer, B. Aurand, V. Bagnoud, J. Fils, T. Kuhl, X. X. Lin, C. Li, Y. T. Li, M. Roth, D. Neely, and P. McKenna, Appl. Phys. Lett. **99**, 171502 (2011).
[21] S. P. D. Mangles, Ph.D. thesis, Imperial College, London, 2005.
[22] M. Lezius, S. Dobosz, D. Normand, and M. Schmidt, Phys. Rev. Lett. **80**, 261 (1998).
[23] FUJIFILM. http://www.fujifilm.com, April 2013.
[24] G. Fiksel, F. J. Marshall, C. Mileham, and C. Stoeckl, Rev. Sci. Instrum. **83**, 086103 (2012).
[25] D. Taylor, E. Liang, T. Clarke, A. Henderson, P. Chaguine, X. Wang, G. Dyer, K. Serratto, N. Riley, M. Donovan, and T. Ditmire, High Energy Density Phys. **9**, 363 (2013).
[26] S. Cipiccia, M. R. Islam, B. Ersfeld, R. P. Shanks, E. Brunetti, G. Vieux, X. Yang, R. C. Issac, S. M. Wiggins, G. H. Welsh, M.-P. Anania, D. Maneuski, R. Montgomery, G. Smith, M. Hoek, D. J. Hamilton, N. R. C. Lemos, D. Symes, P. P. Rajeev, V. O. Shea, J. M. Dias, and D. A. Jaroszynski, Nat. Phys. **7**, 867 (2011).
[27] S. Kneip, S. R. Nagel, C. Bellei, N. Bourgeois, A. E. Dangor, A. Gopal, R. Heathcote, S. P. D. Mangles, J. R. Marquès, A. Maksimchuk, P. M. Nilson, K. T. Phuoc, S. Reed, M. Tzoufras, F. S. Tsung, L. Willingale, W. Mori, A. Rousse, K. Krushelnick, and Z. Najmudin, Phys. Rev. Lett. **100**, 105006 (2008).
[28] S. Kneip, S. R. Nagel, S. F. Martins, S. P. D. Mangles, C. Bellei, O. Chekhlov, R. J. Clarke, N. Delerue, E. J. Divall, G. Doucas, K. Ertel, F. Fiuza, R. Fonseca, P. Foster, S. J. Hawkes, C. J. Hooker, K. Krushelnick, W. B. Mori, C. A. J. Palmer, K. Ta Phuoc, P. P. Rajeev, J. Schreiber, M. J. V. Streeter, D. Urner, J. Vieira, L. O. Silva, and Z. Najmudin, Phys. Rev. Lett. **103**, 035002 (2009).
[29] I. H. Hutchinson, *Principles of Plasma Diagnostics* (Cambridge University Press, Cambridge, England, 2002).

[30] A. A. Ovsyannikov and M. F. Zhukov, *Plasma Diagnostics* (Cambridge International Science, Cambridge, England, 2005).

[31] A. P. L. Robinson, R. M. G. M. Trines, J. Polz, and M. Kaluza, Plasma Phys. Controlled Fusion **53**, 065019 (2011).

[32] S. C. Wilks, A. B. Langdon, T. E. Cowan, M. Rooth, M. Singh, S. Hatchett, M. H. Key, D. Pennington, A. MacKinnon, and R. A. Snavely, Phys. Plasmas **8**, 542 (2001).

[33] S. Hatchett, C. G. Brown, T. E. Cowan, E. A. Henry, J. S. Johnson, M. H. Key, J. A. Koch, A. B. Langdon, B. F. Lasinski, R. W. Lee, A. J. Mackinnon, D. M. Pennington, M. D. Perry, T. W. Phillips, M. Rooth, T. C. Sangster, M. K. Singh, R. A. Snavely, M. A. Stoyer, S. C. Wilks, and K. Yasuike, Phys. Plasmas **7**, 2076 (2000).

[34] N. Naseri, S. G. Bochkarev, and W. Rozmus, Phys. Plasmas **17**, 033107 (2010).